This is a repository copy of *The evolution of ice fabrics: A continuum modelling approach validated against laboratory experiments*.

White Rose Research Online URL for this paper:
https://eprints.whiterose.ac.uk/168885/

Version: Accepted Version

The evolution of ice fabrics: A continuum modelling approach validated against laboratory experiments

Daniel H. M. Richards

Samuel S. Pegler

Sandra Piazolo

Oliver G. Harlen

There remains a significant challenge to model ice crystal fabrics both accurately and efficiently within ice-sheet models. We develop the first fully constrained continuum model, validated against experiments, able to predict the evolution of a crystal fabric for any flow field or temperature. For this, we apply a mesoscopic continuum model describing the evolution of a mass distribution function of c-axis orientations. The model assumes that ice deforms by dislocation creep with slip primarily along the basal plane, and incorporates the effects of rigid body rotation, migration recrystallization and rotational recrystallization. We solve the model using a new spectral method, which is computationally highly efficient. By constraining the model parameters using data from laboratory experiments in simple shear, we provide the first estimates of two fundamental dimensionless parameters controlling the importance of different recrystallization processes as a function of temperature, as well as the first constraints on the strain rate dependence of these parameters. With no further fitting, we apply the model to the case of compression, yielding excellent quantitative agreement with observed fabrics from corresponding experiments. The combination of the model, the spectral method and the parameter constraints as functions of temperature provide accurate and efficient predictions of ice crystal fabric evolution for general deformations, temperatures and strain rates. The model-solver (SpecCAF) can, in principle, be extended to other important polycrystalline materials including olivine, the key material in mantle dynamics.

1   Introduction

Mass loss from ice sheets is set to be the main contributor to sea-level rise this century (Shepherd et al., 2018). In natural flows, ice grains align along preferred directions, creating a strong viscous anisotropy. Ice deformed in uniaxial compression can have a viscosity up to ten times lower than isotropic ice (Pimienta and Duval, 1987; Shoji and Langway, 1988). The ice fabric is an important control on the rheology (Minchew et al., 2018) through the induced viscous anisotropy. However, even state-of-the-art ice-sheet models (Gagliardini et al., 2013; Winkelmann et al., 2011) either neglect the effects of crystal anisotropy or apply a low resolution or unconstrained of fabric that neglect the key process of recrystallisation. Discrete models that solve for the microstructure directly have also been developed and analysed (Montagnat et al., 2014). However, these are both computationally expensive and can fail to produce certain features of ice fabric. There is a need for a reliable, constrained and computationally inexpensive model that can be integrated into large-scale ice-sheet models.

Many laboratory experiments have been performed to investigate CPO development: in uniaxial compression (Craw et al., 2018; Fan et al., 2020; Jacka, 2000; Jacka and Maccagnan, 1984; Montagnat et al., 2015; Piazolo et al., 2013; Qi et al., 2017; Vaughan et al., 2017) and simple shear (Journaux et al., 2019; Qi et al., 2019). This provides a large set of measurements at a range of temperatures, strains and strain rates that could be used to benchmark new models and constrain their underlying parameters.

At a theoretical level, there are also several remaining open questions regarding the development of CPOs in ice. At the microscopic scale, there is still uncertainty over which slip systems and modes of recrystallization are key for producing the CPO patterns observed in nature and the laboratory (Qi et al., 2019). Furthermore, there is only a qualitative, not quantitative, understanding of the importance of different recrystallization processes at different temperatures (Piazolo et al., 2013). The essential effect of strain rate on CPO remains an area of ongoing research (Wilson et al., 2019)

Here, we use a continuum model based on the CAFFE model (Placidi et al., 2010) to model the mass distribution of crystal orientations, which we solve using a spectral method (Montgomery-Smith et al., 2010) originally developed for fibre flows. By solving the inverse problem for the model parameters, we provide the first quantification of the magnitudes of different processes as functions of temperature. This combination provides a fully constrained continuum model for modelling the ice fabric, across a range of temperatures and deformations.

1.1 Processes affecting crystal fabric evolution

The distribution of crystallographic orientations within a polycrystal is called the fabric or crystallographic preferred orientation (CPO). Due to the dominance of basal slip in ice (Duval et al., 2010), we can model the CPO by considering only the normal to the basal plane, referred to as the c-axis. As ice flows, the c-axes align to produce a CPO from the combination of deformation and recrystallization. Figure 1 illustrates schematically the deformation and recrystallization processes that affect the fabric: basal slip deformation, rigid body rotation, rotational recrystallization and migration recrystallization, which we will describe in turn below. For each, the effect on the microstructure is shown above a diagram, referred to as a pole figure, in which the colour indicates the mass distribution of c-axis orientations projected onto a plane. Since the pole figures are antipodally symmetric, it shows all the orientation information.

At typical temperatures for an ice sheet ($-30°$ C to $-5°$ C) slip along the basal plane dominates (Duval et al., 2010). However, non-basal slip can account for up to 30% of deformation in some cases (Chauve et al., 2017). Basal-slip deformation (Figure 1a) can be understood through an analogy to a *deck of cards* sliding over one another causing c-axes to rotate towards the axis of compression (Azuma and Higashi, 1984; van der Veen and Whillans, 1994). A corresponding pole figure of the mass distribution of c-axis orientations shows the movement of a cluster of c-axes towards the compression axis. Furthermore, any vorticity in the flow acts to rotate the c-axes around the axis of vorticity (Figure 1b).

Rotation and migration recrystallization are significant processes in flowing ice (Faria et al., 2014). During rotation recrystallisation (Figure 1c), sub-grains form close to the grain boundaries due to localized stress concentrations (Drury and Urai, 1990). The sub-grains are smaller than their parent grains and have a similar but slightly different orientation. With increasing strain, the sub-grains rotate successively away from the orientation of their parent grain. Consequently, rotational recrystallization can be represented in a pole figure (Figure 1c) as an outwards diffusion of the mass distribution of c-axis orientations away from the initial orientations $\boldsymbol{n}_{1,2,3}$.

Figure 1d illustrates migration recrystallization through the process of grain-boundary migration. Grains with a lower dislocation density with a c-axis orientated towards a given direction $\boldsymbol{n}_1$ will grow into neighbouring grains with higher dislocation densities with directions $\boldsymbol{n}_2$. Migration is driven by the difference in deformation energy between the grains stored in the dislocations (Drury and Urai, 1990). Consequently, the mass fraction orientated towards $\boldsymbol{n}_1$ increases and the mass fraction towards $\boldsymbol{n}_2$ decreases. Migration recrystallization has a similar effect as nucleation of new grains. The probability for a new grain to nucleate and survive is highly dependent on its orientation. "Soft" orientations, which allow easy crystal slip and hence do not accumulate high dislocation densities, are

favoured. Consequently, the distinct phenomena of grain boundary migration and nucleation have a similar effect on the evolution of the orientation space (Cyprych et al., 2016).

1.2   Crystal fabric and ice flow modelling approaches

There are currently several approaches for modelling the CPO of ice. Llorens et al. (2016) model the microstructure directly using a discrete model incorporating deformation and recrystallization processes. This involves simulating both individual grains and the interactions between them. Any deformation is imposed as a boundary condition. Kennedy and Pettit (2015) take a similar approach by modelling a network of cuboids with each cuboid representing an individual grain. These approaches are key to improving our understanding of the processes that lead to CPO formation. However, since they require solving for the microstructure directly ($\sim 10^{-3}$ m), they are too computationally expensive to be incorporated into models of ice sheet flows ($\sim 10^5$ m). Furthermore, they are unable to reproduce some commonly observed patterns seen in experiments and nature, including the secondary c-axis cluster commonly seen in pole figures for simple shear.

Bargmann et al. (2012) used the CAFFE model (Placidi et al., 2010) with rotational and migration recrystallization to model the evolution of ice fabric at an ice divide. The model was implemented using a finite-volume method. They found good agreement up to intermediate depths, before encountering instabilities in their numerical model. In compression, their scheme reproduced cone-shape fabrics, but was unable to reproduce a secondary cluster in shear due to the numerical instabilities. They provided order of magnitude estimates for the model parameters.

At a larger scale there are ice-sheet flow models, which are key to predicting future sea-level rise. However, many models such as PISM (Winkelmann et al., 2011), ISSM (Larour et al., 2012) and others (Cornford et al., 2013; Lipscomb et al., 2018) do not include viscous anisotropy. Elmer/Ice (Gagliardini et al., 2013) incorporates anisotropy, and calculates the CPO development using an evolution equation for the second moment of the CPO distribution function (the second-order orientation tensor), without recrystallization. This approach is computationally inexpensive and can easily accommodate different deformations but cannot accurately reproduce experimentally observed CPOs. The anisotropic viscosity is directly related to the CPO. Therefore, modelling the CPO accurately is key to modelling viscous anisotropy reliably.

2   Model details

To model CPO development, we use the continuum approach of Faria (2006) and Placidi et al. (2010), in which we track the evolution of a distribution function of orientations. The

model tracks quantities over both macroscopic position x and orientation space n. This is based on the theory of *mixtures of continuous diversity* (Faria, 2001) that considers ice as a mixture of grains possessing different orientations. Orientations can be defined by the vector $n(\theta, \varphi)$ in spherical coordinates:

$$n = \sin\theta\cos\varphi\, e_1 + \sin\theta\sin\varphi\, e_2 + \cos\theta\, e_3, \tag{1}$$

where θ is is the polar angle, φ is the azimuthal angle and $\{e_1, e_2, e_3\}$ is a fixed orthonormal basis.

The model makes two continuum assumptions: first that, within any parcel of fluid in macroscopic space x, there are many grains. Second, within any solid angle in orientation space n, there are also many grains. This means that any inhomogeneities at the grain scale are smeared out in orientation space, and we can assume that the velocity is a function of space only and not orientation. This assumption should be valid provided that the ice is deforming by dislocation creep (Faria et al., 2008).

In this section, we retain the generality of the equations in order to demonstrate their versatility and applicability towards large-scale ice-sheet flow models. Afterwards we will apply them to model ice deformed in laboratory experiments, where the variation in macroscopic space x is negligible.

2.1 CPO evolution

We model the CPO using the *orientation mass density*, ρ^*, defined by Faria (2006) as

$$\rho(x, t) = \int_{S^2} \rho^*(x, t, n)\, \mathrm{d}n. \tag{2}$$

Here, $\rho^*\mathrm{d}n$ is the mass fraction of grains with orientations towards n within the solid angle $\mathrm{d}n$ (Placidi et al., 2010). It should be noted that ρ^* describes the mass distribution of orientations, in contrast to the common definition of the orientation distribution function in glaciology (Gagliardini et al., 2009), which describes the number distribution. Except for the unit orientation vector n, we denote all quantities that vary over orientation space by an asterisk. To model the evolution of the orientation density, we apply the model specified by Placidi et al. (2010):

$$\frac{\partial \rho^*}{\partial t} + \nabla \cdot [\rho^* u] = -\nabla^* \cdot [\rho^* v^*] + \lambda \nabla^{*2}(\rho^*) + \beta(\mathcal{D}^* - \langle \mathcal{D}^* \rangle)\rho^*. \tag{3}$$

In this equation, $u(x, t)$ is the macroscopic velocity field, and ∇^* is the gradient operator in orientation space defined by

$$\nabla^* \boldsymbol{v}^* = \frac{\partial \boldsymbol{v}^*}{\partial \boldsymbol{n}} - \left(\frac{\partial \boldsymbol{v}^*}{\partial \boldsymbol{n}} \cdot \boldsymbol{n} \right) \boldsymbol{n} = \frac{\partial v_i^*}{\partial n_j} - \frac{\partial v_i}{\partial n_l} n_l n_j. \tag{4}$$

(the gradient operator restricted to the surface of a sphere). The parameters λ and β represent coefficients controlling the rates of rotational recrystallization and migration recrystallization respectively. The orientationally dependent term $\mathcal{D}^*$ will be defined later in eq. (6). The term $\boldsymbol{v}^*$ defines the orientation transition rate, defined by Placidi et al. (2010) as

$$v_i^* = W_{ij} n_j - \iota \left[D_{ij} n_j - n_i n_j n_k D_{jk} \right]. \tag{5}$$

Here $\mathbf{W} = (\nabla \boldsymbol{u} - \nabla \boldsymbol{u}^T)/2$ is the vorticity tensor and $\mathbf{D} = (\nabla \boldsymbol{u} + \nabla \boldsymbol{u}^T)/2$ is the strain rate tensor. If this equation is applied to an individual grain, it describes the c-axis rotation rate (Gödert and Hutter, 1998; Svendsen and Hutter, 1996) under the Taylor hypothesis (neglecting grain-grain interactions). However, since we are using a continuum model that assumes a large number of grains within any solid angle of orientation, any grain-grain interactions are smeared-out (Faria et al., 2008). In this continuum model, we do not therefore require the Taylor hypothesis.

The first term in eq. (5) represents the effect of vorticity on the CPO (Figure 1b). The second term models basal-slip deformation (Figure 1a). The non-dimensional parameter ι represents the ratio of basal-slip deformation to vorticity induced the rigid-body rotation induced by vorticity. If $\iota = 1$ then the rotation caused by vorticity and basal-slip deformation are of equal magnitude. However, ι is free to take values not equal to 1. For $\iota < 1$ the effect of basal-slip deformation is weaker than rigid-body rotation and vice versa. Previous work (Placidi and Hutter, 2006; Seddik et al., 2008) suggests that $\iota \approx 0.5$ fits data from ice core samples. Because the activity of different slip systems in ice varies with temperature, we expect ι to be a function of temperature.

The parameter λ (s^{-1}) in eq. (3), represents the rate of the rotational recrystallization, which, as shown in Figure 1c and discussed above, can be modelled by a diffusion in orientation space (Gödert, 2003). Migration recrystallization is modelled by an orientation-dependent source term, with the rate controlled by β (s^{-1}). The orientation dependence is governed by the deformability, defined by

$$\mathcal{D}^* = 5 \frac{(D_{ij} n_j)(D_{ik} n_k) - (D_{ij} n_j n_i)^2}{D_{mn} D_{nm}}. \tag{6}$$

Placidi et al. (2010) gives the physical interpretation of $\mathcal{D}^*$ as the (normalised) square of the resolved shear strain rate on the basal plane. As ice deforms primarily by basal slip, the resolved shear rate on the basal plane also drives the accumulation of deformation energy in the grain, which drives migration recrystallization. The average of $\mathcal{D}^*$ is defined as:

$$\langle \mathcal{D}^* \rangle = \int_{S^2} \frac{\rho^*}{\rho} \mathcal{D}^* \; d\boldsymbol{n}.$$

If $\mathcal{D}^*$ is greater than the average value $\langle \mathcal{D}^* \rangle$ then ρ^* at that orientation will increase, modelling grains growing or nucleating with this orientation. Note that the total production and consumption of ρ^* always balance. The factor of 5 is a convention. Since the parameters λ and β represent recrystallization rates, they can be expected to be functions of temperature (Wilson et al., 2019) and strain rate (Piazolo et al., 2013). To date, the only determination of these parameters is an order of magnitude estimate given by Bargmann et al. (2012), without any temperature or strain rate dependence. In this paper we will determine the first detailed constraints on these functions using experimental data from compression and simple shear deformations of ice.

Equation (3) can be used to predict CPO evolution. Unlike models that solve for the microstructure directly, this equation can be applied readily to any velocity field. However, the accuracy of this method is dependent on correctly including the magnitudes of the terms modelling recrystallization, which we will come to later.

2.2 Spectral method

Equation (3) is challenging to solve directly due to the differential operators on the surface of a sphere. In this section we describe a new spectral model, adapted from work by Montgomery-Smith et al. (2010) for fibre flows. The spectral method converts the partial differential equations over orientation space into a system of ordinary differential equations. This allows eq. (3) to be solved with high precision and computational efficiency.

The orientation mass density can be represented in terms of the spherical harmonics:

$$\rho^*(\boldsymbol{x}, t, \boldsymbol{n}) = \sum_{l=0}^{\infty} \sum_{m=-l}^{l} \hat{\rho}_l^m(\boldsymbol{x}, t) Y_l^m(\theta, \varphi), \tag{7}$$

where Y_l^m are spherical harmonic functions. By integrating over the surface of the sphere and multiplying by the complex conjugate $\bar{Y}_l^m$, we obtain the so-called weak form of eq. (4):

$$\left(\frac{\partial}{\partial t} + \boldsymbol{u} \cdot \nabla \right) \int_{S^2} \rho^* \bar{Y}_l^m = \int_{S^2} \nabla^* \cdot (\rho^* \boldsymbol{v}^*) \bar{Y}_l^m + \lambda \nabla^{*2} \rho^* \bar{Y}_l^m + \beta (\mathcal{D}^* - \langle \mathcal{D}^* \rangle) \rho^* \bar{Y}_l^m d\boldsymbol{n}, \tag{8}$$

where we have used incompressibility ($\nabla \cdot \boldsymbol{u} = 0$) to rearrange the left-hand side. By replacing ρ^* in eq. (8) with the spherical harmonic expansion (eq. 7), we can calculate the overlap integrals with $\bar{Y}_l^m$, taking advantage of the orthogonality of spherical harmonics.

Furthermore, we use integration by parts on the surface of a sphere (Montgomery-Smith et al., 2010), to rearrange eq. (8) so the differential operator acts on $\bar{Y}_l^m$:

$$\left(\frac{\partial}{\partial t} + \boldsymbol{u} \cdot \nabla\right)\hat{\rho}_l^m = \int_{S^2} ((2\boldsymbol{n} - \nabla^*)\bar{Y}_l^m) \cdot \boldsymbol{v}^*\rho^* + \beta(\mathcal{D}^* - \langle \mathcal{D}^* \rangle)\bar{Y}_l^m \rho^* \mathrm{d}\boldsymbol{n} - \lambda l(l+1)\hat{\rho}_l^m. \quad (9)$$

Here we have also used the identity $\nabla^{*^2} Y_l^m = -l(l+1)Y_l^m$ to simplify the rotational recrystallization term. The advantage of this form is that differentiation and multiplication by $\boldsymbol{n}$ on $\bar{Y}_l^m$ can be represented as multiplications by other moments of the spherical harmonics through ladder operators (Montgomery-Smith et al., 2010). This allows eq. (9) to be rewritten as the ordinary differential equation:

$$\left(\frac{\partial}{\partial t} + \boldsymbol{u} \cdot \nabla\right)\hat{\rho}_l^m = \sum_{l'=0}^{\infty} \sum_{m'=-l'}^{l'} C_{l,l'}^{m,m'} \hat{\rho}_{l'}^{m'}, \quad (10)$$

where the unknowns in $C_{l,l'}^{m,m'}$ can be found using the algorithm described in Montgomery-Smith et al. (2010), which recursively replaces any operation or multiplication acting on the spherical harmonics until it can be expressed in terms of higher or lower order harmonics. This involves the use of Rodrigues' Formula which gives the effect of multiplying any Y_l^m by $\boldsymbol{n}$, and ladder operators for differentiation. The reader is referred to Montgomery-Smith et al. (2010) for a detailed derivation.

In our numerical method, we truncate the outer summation in eq. (10) at $l' = L$, where L is a positive integer representing the number of harmonics used. A comparison of the truncation error for different values of L is given in Appendix A. Truncating at L gives the same precision as solving the evolution equation for the Lth-order orientation tensor.

The combination of the equations and the spectral method, which we call SpecCAF, give a versatile, accurate and efficient method for predicting CPO evolution with all key processes, which could be extended to other polycrystalline materials apart from ice.

2.3 Non-dimensionalisation

Before working with eq. (3) we non-dimensionalise to reduce the number of variables in the system and to allow us to compare experiments performed at different scales and strain rates more effectively. In modelling the configuration of the laboratory experiments, we assume that the fabric is spatially homogeneous ($\nabla\rho^* = 0$) such that there is no spatial lengthscale, and the strain rate is constant. The ice has a mass density ρ_o and, for a given

deformation, we assume a characteristic strain rate $\dot{\gamma}$ (with units s^{-1}). The non-dimensional variables are represented with tildes and are defined as:

$$\tilde{\rho}^* = \frac{\rho^*}{\rho_0}, \quad \tilde{\mathbf{D}} = \frac{\mathbf{D}}{\dot{\gamma}}, \quad \tilde{\mathbf{W}} = \frac{\mathbf{W}}{\dot{\gamma}}$$

$$\tilde{\lambda}(T,\dot{\gamma}) = \frac{\lambda(T,\dot{\gamma})}{\dot{\gamma}}, \quad \tilde{\beta}(T,\dot{\gamma}) = \frac{\beta(T,\dot{\gamma})}{\dot{\gamma}}$$

Recasting eq. (3) in terms of the non-dimensional variables above, we obtain :

$$\frac{\partial \tilde{\rho}^*}{\partial \tilde{t}} = -\nabla^* \cdot [\tilde{\rho}^* \tilde{\boldsymbol{v}}^*] + \tilde{\lambda}(T,\dot{\gamma})\nabla^{*2}(\tilde{\rho}^*) + \tilde{\rho}^* \tilde{\beta}(T,\dot{\gamma})(\mathcal{D}^* - \langle \mathcal{D}^* \rangle), \tag{11}$$

where

$$\tilde{v}_i^* = \tilde{W}_{ij} n_j - \iota(T)\left[\tilde{D}_{ij} n_j - n_i n_j n_k \tilde{D}_{jk}\right]$$

is the non-dimensional form of the orientation transition rate (eq. (5)). The governing equation depends on three dimensionless parameters. Physically, $\tilde{\lambda}$ represents the ratio of the rate of rotational recrystallization to the strain rate, and $\tilde{\beta}$ represents the ratio of the rate of migration recrystallization to the strain rate. The ratio of basal-slip deformation to rigid-body rotation, $\iota(T)$ is already non-dimensional so is not modified. The non-dimensional time is $\tilde{t} = \dot{\gamma}t$.

3 Results

We use the model to compare to laboratory experiments of ice deformed in uniaxial compression and simple shear. We apply the model with $L = 12$ and apply a Runge-Kutta scheme for the time integration.

3.1 General forms of CPO

We begin with an overview of the fabrics produced by the model in four different modes of deformation. Figure 2 shows both sketched pole figures and predicted pole figures obtained from the model for each form of deformation at a true strain of $\gamma = 0.7$. Panels (a)-(d) of Figure 2 illustrate the typical CPOs predicted by the model, with and without migration recrystallization, under respectively: uniaxial compression ($\nabla \tilde{\boldsymbol{u}} = \text{diag}(0.5, 0.5, -1)$), pure shear ($\nabla \tilde{\boldsymbol{u}} = \text{diag}(1,0,-1)$), uniaxial extension ($\nabla \tilde{\boldsymbol{u}} = \text{diag}(1, -0.5, -0.5)$), and simple shear,

$$\nabla \tilde{\boldsymbol{u}} = \begin{bmatrix} 0 & 0 & 1 \\ 0 & 0 & 0 \\ 0 & 0 & 0 \end{bmatrix}.$$

The colour in the pole figures represents the magnitude of $\tilde{\rho}^*$ at that orientation. The pole figure is plotted with an azimuthal equidistant projection. For these examples, illustrative values of $\tilde{\lambda} = 0.03$, $\iota = 1$ and $\tilde{\beta} = 0$ or 2 were used. The right-hand column shows a pole figure of the deformability, $\mathcal{D}^*$, highlighting which orientations are favoured for grain growth by migration recrystallization.

In uniaxial compression (Figure 2a) without migration recrystallization, basal-slip deformation produces a single-maximum fabric towards the axis of compression. For this deformation, migration recrystallization acts to produce grains orientated at 45° to the z-axis, and consume grains orientated otherwise. The balance between this process and basal-slip produces a cone-shape CPO with a cone angle of $< 45°$. The model produces the expected single-maximum or cone-shape fabric depending on whether migration recrystallization is included.

For pure shear (Figure 2b) the single maximum is elongated without migration recrystallization, and this feature is present in the model. With migration recrystallization, instead of a cone-shape seen in Figure 2a, two separate maxima develop, which can be seen in both the sketch and the model.

For uniaxial extension (Figure 2c) the model again agrees with the sketched pole figures. Without migration recrystallization, a girdle fabric is produced in the yz-plane. Migration recrystallization transforms the girdle fabric into a cone-shape fabric with the axis of the cone in the x-direction.

Simple shear (Figure 2d) is the only flow with non-zero vorticity. Therefore, the orientation transition rate contains contributions from both rigid-body rotation and basal-slip deformation. The model predicts a single maximum orientated at a certain angle slightly offset from the shear plane, set by the balance between vorticity and basal-slip deformation. The sketch from observations, however, shows a single maximum with no offset. Migration recrystallization produces orientations towards the z and x directions. The cluster at the z-axis is sustained by a balance between vorticity moving it to the right, basal-slip deformation moving to the left and migration recrystallization acting as a source term. For the cluster orientated towards the $-x$-axis, vorticity and basal-slip deformation both act to move it in the same direction. Once these grains are no longer orientated towards the x-axis migration recrystallization causes grains more favourably orientated, i.e. those towards the x or z-axes, to consume them. This results in the secondary cluster gradually weakening.

3.2 Strain rate dependence

We now investigate the strain rate dependence of the ice fabric development. We investigate how key measures of the CPO, λ_1, the largest eigenvalue of $\mathbf{A}^{(2)}$, and J, a measure of total fabric concentration,$\tilde{\rho}^*)^2$ d$\boldsymbol{n}$

$$J = \int_{S^2} (\tilde{\rho}^*)^2 \, \mathrm{d}\boldsymbol{n},$$

change with strain rate. These changes are shown in Figure 3 for experiments in uniaxial compression (Craw et al., 2018; Piazolo et al., 2013). For temperatures and strains at which there are multiple experiments the data has been sorted into bins (shown in the legend) and normalised by the value at $\dot{\gamma} = 2.5 \times 10^{-6}$ s^{-1} for each bin. This allows experiments from different temperatures and strains to collapse onto a single curve and, to first approximation, a power-law fit to be performed. As can be seen from Figure 3 and the value of the derived power law exponents, both λ_1 and J depend very weakly on strain rate. For example, the value of λ_1 varies by only ~12% over two orders of magnitude of strain rate. This highlights how the CPO has only very weak dependence on strain rate.

We can extend our hypothesis of modelling strain rate dependence by a power law to the recrystallization parameters:

$$\lambda \propto \dot{\gamma}^a, \quad \tilde{\lambda} \propto \dot{\gamma}^{a-1}, \quad \beta \propto \dot{\gamma}^b, \quad \tilde{\beta} \propto \dot{\gamma}^{b-1}. \tag{12}$$

Based on the weakness of the strain rate dependence in Figure 3 we can assume with confidence that to leading order $a, b \approx 1$ in eq. (12). This means that the CPO and non-dimensional parameters can be assumed to be independent of strain rate (for ranges typical of experiments and applications).

3.3 Inversion for parameters in simple shear

Based on the assumed strain rate independence above, we henceforth assume that the three non-dimensional parameters in the model $\left(\tilde{\lambda}, \tilde{\beta}, \iota \right)$ are functions of temperature only. To provide the first quantification of these dependences, we apply a regression to invert the model for the parameters $\left(\tilde{\lambda}, \tilde{\beta}, \iota \right)$ that give the best fit to experimental data (Journaux et al., 2019; Qi et al., 2019). We begin by conducting this inversion using experiments of simple shear. Once these parameters are constrained for this case, we use them to compare the model to experimental data in compression, thereby checking the predictive accuracy of the model for generalised deformations without any further fitting.

Qi et al. (2019) deformed ice cores in direct simple shear. The ice had an initially isotropic fabric and was deformed at temperatures of $-30°$ C, $-20°$ C and $-5°$ C, at a constant strain rate of 10^{-4} s^{-1} up to strains of $\gamma = 2.6$. They found the development of a secondary

cluster in all experiments except at high strain and $-30°$ C. They hypothesise these patterns arise from the balance between lattice rotation and migration recrystallization.

Journaux et al. (2019) ran similar experiments but deformed the ice in torsion at $T = -7°$ C and a mean strain rate of $\dot{\gamma} = 1.14 \times 10^{-6}$ s^{-1} over a range of strains. This still produces the same form of simple-shear deformation as that of Qi et al. (2019).

In order to invert for the model parameters $(\tilde{\lambda}, \tilde{\beta}, \iota)$ as functions of temperature, we fitted the model to the CPOs from simple shear experiments. We minimised the total difference in the unique components of the fourth-order orientation tensor between the model and experiments. Data from experiments at $-20°$ C in Qi et al. (2019) was not included because only two experiments were performed at this temperature, so it is difficult to constrain the parameter set. Once the parameters $(\tilde{\lambda}, \tilde{\beta}, \iota)$ were found over a range of temperatures, we performed a linear regression to obtain these parameters as functions of temperature, which is plotted in Figure 4. The parameters ι and $\tilde{\beta}$ both increase with temperature, highlighting increased basal-slip deformation and migration recrystallization. However, rotational recrystallization, controlled by $\tilde{\lambda}$, is fairly constant.

Figure 5 shows a comparison of the model and experiments in both simple shear and uniaxial compression. The parameters at each temperature were calculated from the linear regression in Figure 4. There is excellent agreement between the model and experiments, across deformations, temperature and strain rate. As an initial condition we assume an isotropic fabric, i.e. $\tilde{\rho}^* = 1/4\pi$ everywhere. The plot on the left shows the largest two eigenvalues of the second-order orientation tensor,

$$A_{ij}^{(2)} = \langle n_i n_j \rangle \equiv \int_{S^2} \tilde{\rho}^* \, n_i n_j \, \mathrm{d}\boldsymbol{n} \tag{13}$$

 for the model and experiments. The experimental strain rates are visualised by the size of the circles. The numbered experiments are plotted as pole figures, alongside a pole figure extracted from the model at the same strain. The results demonstrate the ability of the model to accurately model fabric evolution in different deformations and its strong dependence on temperature.

For simple shear in Figure 5a the plot of the largest two eigenvalues $\mathbf{A}^{(2)}$ against shear strain γ shows the largest eigenvalue increasing , corresponding to the cluster orientated towards the z-axis. The model accurately tracks the evolution seen in the experiments, including for the simulation at $T = -20°$ C which was not used in the inversion.

We can accurately reproduce the experimental CPOs across a range of temperatures and strain rates. The model reliably predicts a secondary cluster, commonly seen at lower strains such as experiments (3), (5), and (7) in Figure 5a, presenting the first theoretical

demonstration of this feature. At higher strains the secondary cluster begins to disappear, such as in (4) and (6), in direct agreement with the model predictions.

The data for experiments at $-7°$ C is from Journaux et al. (2019). As can be seen from the size of the circles in Figure 5a, these experiments were performed at a lower strain rate ($\dot{\gamma} = 10^{-7} - 10^{-6}$ s^{-1}). Despite the multiple orders of magnitude difference in strain rate from Qi et al. (2019) the model and parameters, without strain rate dependence, still show excellent agreement with the experimental results.

3.4 Extrapolation to compression

To test the model in a different deformation configuration, we applied it in the case of uniaxial compression and compared it to experiments (Craw et al., 2018; Piazolo et al., 2013). with no further fitting. The parameters $\left(\tilde{\lambda}, \tilde{\beta}, \iota\right)$ were taken from the linear regression performed in simple shear (Figure 4). Note Piazolo et al. (2013) used D_2O ice hence the temperatures have been converted based on the difference in melting points (Ossipyan and Petrenko, 1988). The experiments are over a greater variety of strain rates ranging compared to the simple shear experiments, ranging from $\dot{\gamma} = 6 \times 10^{-7} - 2.4 \times 10^{-4}$s^{-1}.

The comparison between the model and experiments is shown in Figure 5b. For uniaxial compression we plot the largest two eigenvalues of $\mathbf{A}^{(2)}$against true axial strain ε. The growth of the largest eigenvalue represents the concentration of orientation towards the z-axis. The presence of a cone-shape fabric cannot be discerned from $\mathbf{A}^{(2)}$. The agreement between the model and experiments seen here is excellent, with the model lying within the experimental scatter at all temperatures. The model also predicts the rapid development of a CPO even at very low strains.

At $T = -30°$ C the model pole figures agree well with experiments. Both experiments (9) and (10) show a large asymmetry in the pole figure which can be assumed to be due to experimental scatter. At $T = -20.5°$ C and $T = -13.6°$ C, the model consistently predicts a cone-shape fabric even at low strains. However, there is a small disagreement as only experiment (13) has a cone-shape fabric, and (11) and (12) do not. At the higher temperature of $T = -10°$ C, a cone-shape is seen in both experiments and the model.

Figure 6 shows how cone angle changes with temperature and strain. A range of laboratory experiments are plotted as circles, with the colour representing the experimental temperature and the strain rate shown by the size, as before. The model was run at different temperatures and plotted alongside as solid lines.

Again, there is excellent agreement with experiments. There is scatter in the experiments, but the model generally predicts the trend of cone angle reducing gradually as strain

increases for $-15 < T < -5°$ C. We also accurately predict the decrease in cone angle at $-30°$ C, including the point at which the fabric transitions from a cone-shape to a single-maximum (corresponding to $\theta = 0°$).

These comparisons show that the model, with the parameters determined earlier in simple shear, also work in uniaxial compression with no further fitting required. As simple shear and uniaxial compression represent end-members of possible deformations, we can expect the model to work for general deformations.

4 Discussion

4.1 General model behaviour

In summary, the model incorporates four processes (Figure 1): basal-slip deformation, rigid-body rotation of the CPO, rotational recrystallization (which acts to diffuse the CPO), and migration recrystallization (which acts as a source or a sink at specific orientations depending on the deformation configuration). By including basal-slip deformation and migration recrystallization (and rigid-body rotation in simple shear) the model is able to reproduce all observed CPOs in existing laboratory experiments. Generally, there is excellent agreement across the different deformations of compression and simple shear, across strain rates ranging from $10^{-7} - 10^{-4}\text{s}^{-1}$ and temperatures ranging from $-30°$ C and $-5°$ C. The excellent agreement indicates that other processes, such as non-basal slip, do not need to be modelled explicitly for accurate prediction of CPO evolution even if they are active in the microstructure.

Figure 4 shows that as temperature increases both ι and $\tilde{\beta}$ increase, while $\tilde{\lambda}$ stays roughly constant. The qualitative increase of migration recrystallization $(\tilde{\beta})$ with temperature agrees with theory (Faria et al., 2014). However, this work is the first numerical quantification of migration recrystallization and its change with temperature. Although it could be expected that the temperature dependence would conform to an Arrhenius equation, we find that a linear relationship gives the best prediction at intermediate values $(T \approx -20°$ C).

The parameter ι, which represents the ratio of basal-slip deformation to rigid-body rotation, increases from ~ 1 at $-30°$ C to ~ 1.6 at $-5°$ C. In comparison, Seddik et al. (2008) found $\iota = 0.6$ best represented CPOs from ice core samples which were at roughly $-40°$ C. They did not posit a temperature dependence. Our regression predicts $\iota \approx 0.9$ at this temperature. The difference can be explained by noting that their model did not include rotation or migration recrystallization.

The use of values of $\iota > 1$ is novel. If ι is capped at 1, the model cannot reproduce the experimental pole figures or the experimental evolution of the orientation tensor. The increased relative contribution from basal slip can be explained by the synchronous increased activity of migration recrystallization at higher temperatures. This means more grains with low dislocation density grow and grains with high dislocation density are consumed. Non-basal slip occurs more frequently in regions of high dislocation density (Chauve et al., 2017). Therefore, migration recrystallization acts to increase the amount of grains favourably oriented for basal slip.

The model predicts that rotational recrystallization, controlled by $\tilde{\lambda}$, is roughly independent of temperature, only increasing by 15% from $-30°$ C to $-5°$ C. This suggests that rotational recrystallization should be primarily stress or strain rate dependent, in broad agreement with the theory of Faria et al. (2014).

The offset single-maximum CPO in simple shear which is shown in Figure 2d with $\tilde{\beta} = 0$ is also captured in models by Llorens et al. (2016) and van der Veen and Whillans (1994) without recrystallization processes. In nature and experiment, this is unlikely to occur as this situation can only arise if $\iota \geq 1$ and $\tilde{\beta} \approx 0$. Such a combination of parameters does not occur at any temperature (Figure 4): for low temperatures $\iota < 1$ and $0 < \tilde{\beta} < 1$ and for high temperatures migration recrystallization is large even though $\iota > 1$.

4.2 Prediction of strain rate dependence

In Figure 4 we have assumed that the non-dimensional parameters are independent of strain rate. This means that the ratio of recrystallization rate to strain rate is effectively constant. As can be seen from Figure 5, this is a good assumption to leading order, and the parameters are able to predict the CPO across a variety of strain rates.

Nevertheless, to provide here the first estimate of the strain rate dependence of the parameters controlling the relative importance of recrystallisation processes in eq. (12), we perform a regression for the parameters $\left(\tilde{\lambda}, \tilde{\beta}, \iota\right)$ including all experimental data, in both compression and simple shear (Table 1). The top half of the table shows the inversion results. The mean temperature T, mean strain rate $\dot{\gamma}$, number of experiments in each set n and coefficients of variances c_v are also shown. For simple shear the parameters were found by minimising the error in the components of $\mathbf{A}^{(4)}$ as described previously. For compression, due rotational symmetry in φ, the error was defined as the θ integral of the difference between φ averaged $\tilde{\rho}^*$:

$$\text{error} = \int_0^{\pi/2} \left| \int_0^{2\pi} \rho_{\text{exp}}^* (\theta, \varphi) \, \mathrm{d}\varphi - \int_0^{2\pi} \rho_{\text{sim}}^* (\theta, \varphi) \, \mathrm{d}\varphi \right| \sin\theta \, \mathrm{d}\theta. \qquad (14)$$

This takes advantage of the rotational symmetry of the CPO in compression to give a more precise measure of the difference between two CPOs. The bottom half of the table shows regressions with and without strain rate dependence. These regressions were performed using all the experimental data shown in Table 1 (both compression and simple shear), hence differ from those of Figure 4. The bottom half of Table 1 shows the fit results, R^2, adjusted R^2 and confidence intervals, to compare regressions with different number of predictors.

The fit for strain rate dependence in Table 1 is the first quantification of how the parameters change with strain rate. Including strain rate dependence widens the confidence intervals for the parameters. Further experiments are required for a more reliable estimate. However, as a first attempt the values are close to what was hypothesised: all parameters have exponents close to zero, highlighting the weakness of the dependence. For ι the exponent is very close to zero (0.002), which supports our hypothesis that the ratio of basal-slip deformation to rigid body rotation are independent of strain rate. Furthermore, our estimate also indicates that $a = p_{\tilde{\lambda}} + 1 > 1$ and $b = p_{\tilde{\beta}} + 1 < 1$ from eq. (12). Therefore, the rate of rotational recrystallization increases with strain rate while the rate of migration recrystallization decreases with strain rate.

4.3   Comparison with other models

In a hierarchy of complexity, this model sits between direct modelling of the polycrystal (Kennedy and Pettit, 2015; Llorens et al., 2016), and the use of orientation tensors (Seddik et al., 2011). The model SpecCAF used here is considerably less expensive computationally than modelling the polycrystal directly, whilst being of comparable cost to solving for orientation tensors. This means that it represents a viable candidate for inclusion in ice-sheet models.

Models such as those employed by Llorens et al. (2016) simulate directly the polycrystal and hence give a more complete representation of the microstructure than included here. However, it is difficult to apply general or changing deformations to these models. Such models are also far too computationally expensive to be used in ice-sheet models. The model used in this paper does not have these disadvantages. Despite this, the results compare favourably with Llorens et al. (2016). We are consistently able to reproduce the secondary cluster seen in experiments, whereas the bulk CPOs produced by Llorens et al. (2016) do not show one, although it does appear in the high strain rate areas for $\gamma < 1$.

To simulate CPOs at an ice divide, Bargmann et al. (2012) used the same CPO evolution equation as this paper but solved with a finite-volume method. They constrained the parameters to an order of magnitude. They found $\tilde{\beta} = O(1)$ and $O(0.01) < \tilde{\lambda} < O(0.1)$, consistent with our results.

For large-scale ice-sheet models, the state-of-the-art for fabric evolution is to calculate the evolution of the second-order orientation tensor without recrystallization (Gagliardini et al., 2013). This is equivalent to setting $\tilde{\beta}, \tilde{\lambda} = 0$ and running SpecCAF with $L = 2$. This is unable to produce any detailed features, including the entire cone-shape CPO in compression or the secondary cluster in simple shear. Therefore, this approach is likely unable to predict the orientation tensors sufficiently accurately to model viscous anisotropy.

4.4   Future Applications

Our contribution of the spectral method and parameter inversion represents a step forward for the accuracy of CPO predictions in ice-sheet models. The model and parameters can take the flow field, temperature and strain rate as inputs and then predict accurately the CPO. The versatility, accuracy and computational efficiency of the model across deformations and temperature make it an excellent candidate for integration into ice-sheet models such as Elmer/Ice (Gagliardini et al., 2013). It should also be noted that, if SpecCAF is incorporated in such models, then the user can adjust the number of spherical harmonics L to balance accuracy against computational cost. For example, although we use L = 12, $L = 6$ in our model, we can still represent a secondary cluster in the CPO (Figure 7).

The framework presented here can also be applied to other geological materials that develop a CPO and viscous anisotropy. The model-solver SpecCAF is transferable to other crystalline materials whose plasticity is dominated by one slip system in a certain temperature range, like mica or quartz (Kronenberg et al., 1990; Schmid and Casey, 1986). SpecCAF could also be generalised to other materials with multiple active slip systems. In this case the combination of our scheme with existing continuum models for slip-dependent CPO development is promising. For example, CPO development in olivine is an important research area: olivine is the main constituent of the upper mantle (Boehler, 1996) and has seismic and viscous anisotropy which is controlled by the CPO (Nicolas and Christensen, 1987). Large scale geodynamic models are highly dependent on the flow of the mantle where viscous anisotropy may play a major role (Tommasi et al., 2009), so accurately predicting CPO development is key for this field.

5   Conclusions

We provide the first complete, fully constrained framework for modelling the CPO for low computational cost, at any temperature including all key processes. This is done by solving the fabric evolution equation by Placidi et al. (2010) using a spectral method adapted from Montgomery-Smith et al. (2010) and then using experimental data in simple shear and compression to constrain the model parameters. The spectral method can solve the equations to high accuracy with low computational cost. The inversion for the model

parameters (Figure 4) provides the first quantitative estimate of the relative importance of different processes which affect the CPO as functions of temperature. The model-solver SpecCAF, combined with these parameters as functions of temperature, gives excellent agreement with experiments across a large range of deformations, temperatures and strain rates.

The model provides new inroads towards understanding ice fabric dynamics under different deformations, for the interpretation of ice cores, and for implementation into ice-sheet models. The model provides the first method to capture all key features of CPOs such as secondary clusters across a range of temperatures and deformations and shows greater accuracy than full field models for much lower computational cost. That these accurate predictions arise mainly from the balance between basal-slip deformation and migration recrystallization highlight the importance of these processes. The constrained model provides a complete toolkit to model dynamically the fabric development in an ice sheet.

SpecCAF could be extended to other crystalline materials with one dominant slip system, such as micas. Furthermore, it could be generalised to incorporate more than one slip system, enabling modelling of more complex polycrystalline materials such as olivine, which is of primary importance to mantle dynamics.

Acknowledgements

Appendix A. Number of harmonics

This appendix illustrates how by varying L in eq. (15), the computational cost and accuracy vary (Figure 7). Both the error, defined as:

$$\text{error} = \frac{\left|\lambda_i^L - \lambda_i^{L=50}\right|}{\lambda_i^{L=50}}, \tag{15}$$

where λ_i^L is the ith largest eigenvalue of $\mathbf{A}^{(2)}$ with L spherical harmonics, and pole figures are shown, all at $\gamma = 1$ in simple shear. Setting $L = 2$ gives similar accuracy to solving the evolution equation for $\mathbf{A}^{(2)}$. As can be seen in the figure, above $L = 8$ there is little difference in the pole figures.

Appendix B. Experimental data used in comparison

This appendix gives Table 2, which shows the key data for each experiment used for comparison in Figure 5.

Figures and Tables
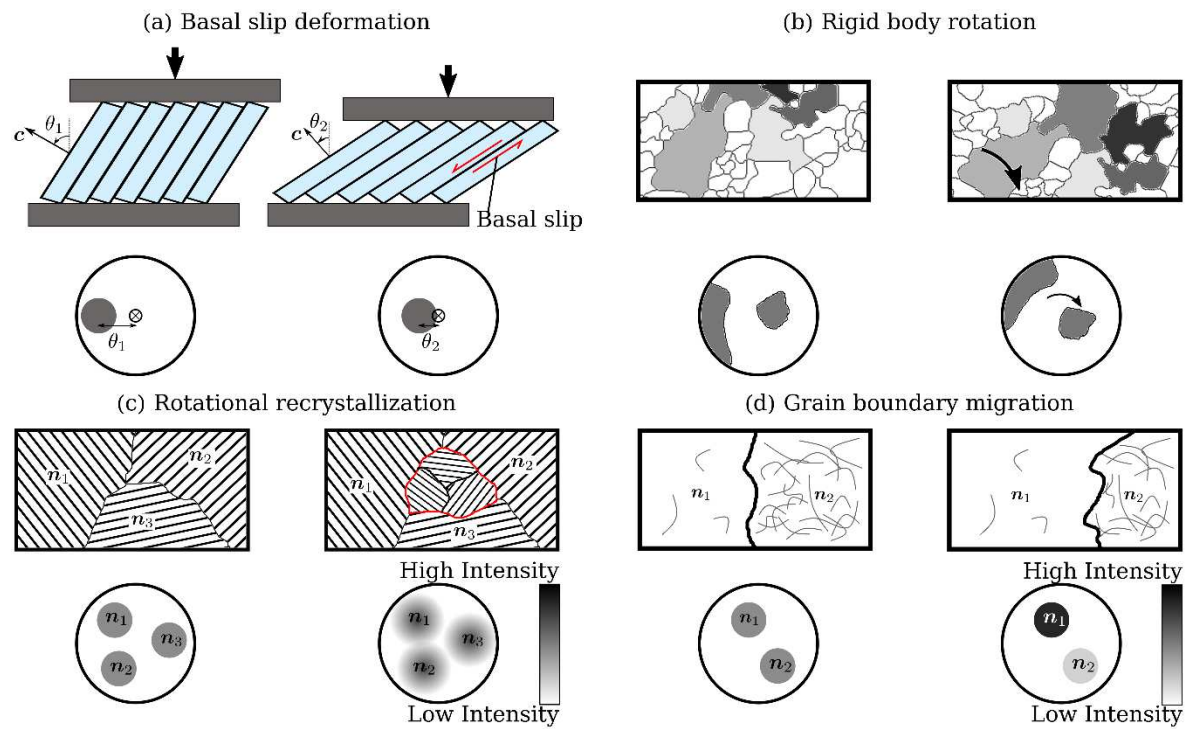
Figure 1: Diagram showing the four processes that can affect the ice CPO. An illustration of the mechanism on the microstructure, as well as the resulting effect on a pole figure of orientation mass distributions is shown for each one. (a) Under basal slip deformation, the c-axis rotates towards the axis of compression. In the pole figure for this case the cluster of c-axes at θ_1 also move towards the compression axis. (b) Rigid body rotation: any vorticity in the flow acts to rotate the crystallites and their c-axes around the axis of rotation. (c) Rotational

recrystallization: $\boldsymbol{n}_{1,2,3}$ represent grains with their orientation illustrated by the direction of hatching. Sub grains form at the boundaries between larger grains with intermediate orientations. In the pole figure, this translates to a diffusion of high intensity clusters of orientation towards: $\boldsymbol{n}_{1,2,3}$. (d) Migration recrystallization: the grain with a lower dislocation density, with orientation n_1, migrates into the grain with a higher dislocation density. In the pole figure, the mass fraction of c-axes towards $\boldsymbol{n}_1$ increases and the mass fraction towards $\boldsymbol{n}_2$ decreases.
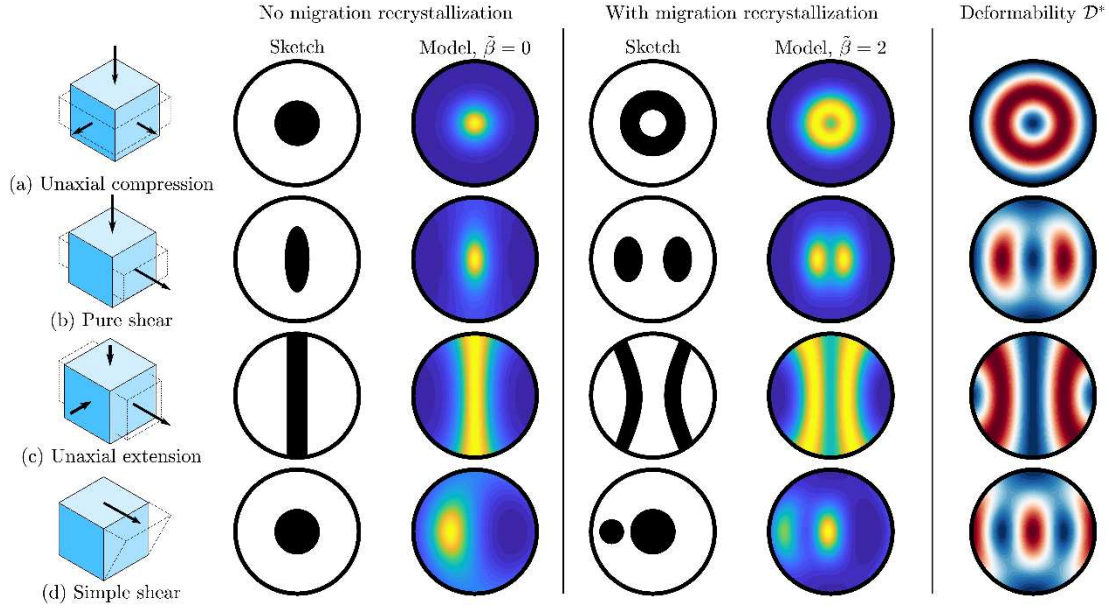
Figure 2: Comparison of the pole-figures produced by the model, compared to sketches of expected pole figures, based on experimental observations and ice core samples (Paterson, 1999). Each row represents a different deformation. Comparison between the expected sketch and the model are presented for both no migration recrystallization, $(\tilde{\beta} = 0)$, and with migration recrystallization, for the illustrative case of $\tilde{\beta} = 2$. Other parameter values chosen were $\tilde{\lambda} = 0.05$ and $\iota = 1$. The model pole figures are plotted at true strain $\gamma = 0.7$. The final column shows a plot of the deformability, $\mathcal{D}^*$ from eq. (6), which controls migration recrystallization.
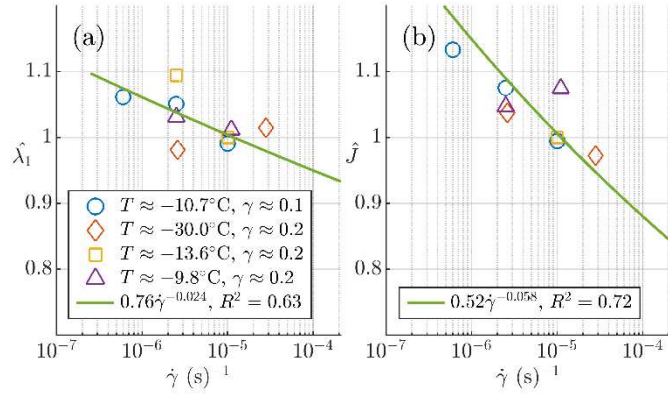
Figure 3: This figure shows the strain rate dependence of experimental CPOs in uniaxial compression. The plots show two measures of CPO concentration for this flow field, λ_1, the largest eigenvalue of $\mathbf{A}^{(2)}$ (a), and $\hat{J}$ (b), against experimental data (Craw et al., 2018; Piazolo et al., 2013). For each data set, in order to identify the strain rate dependence, the values have been sorted into bins with roughly equal temperature ($\pm 1°C$) and strain (± 0.025). The hats indicate the values have been normalised against the value at $\dot{\gamma} = 10^{-5}$ in order to collapse different bins onto a single curve. A fit is also shown along with the R^2 value of the fit.
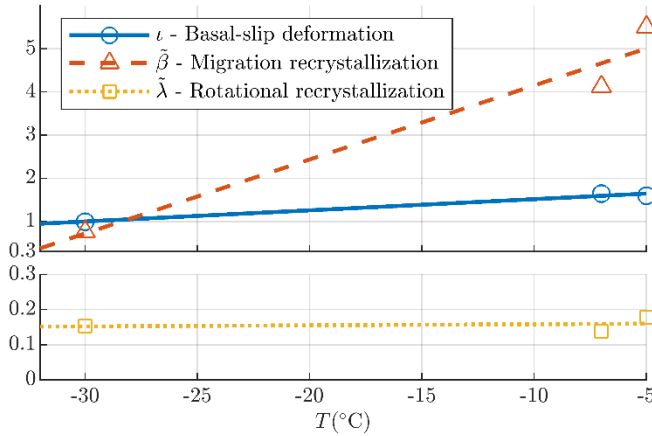
Figure 4: Plot of the parameters $\tilde{\lambda}$ (rotational recrystallization), $\tilde{\beta}$ (migration recrystallization) and ι (basal-slip deformation) found from the inversion described in section 3.3 at three temperatures: $-30, -7, -5°$ C. The inverted-for parameters are shown as points along with a linear regression from these points for each parameter. Note the broken y-axis as the parameter $\tilde{\lambda}$ changes much less than ι and $\tilde{\beta}$.
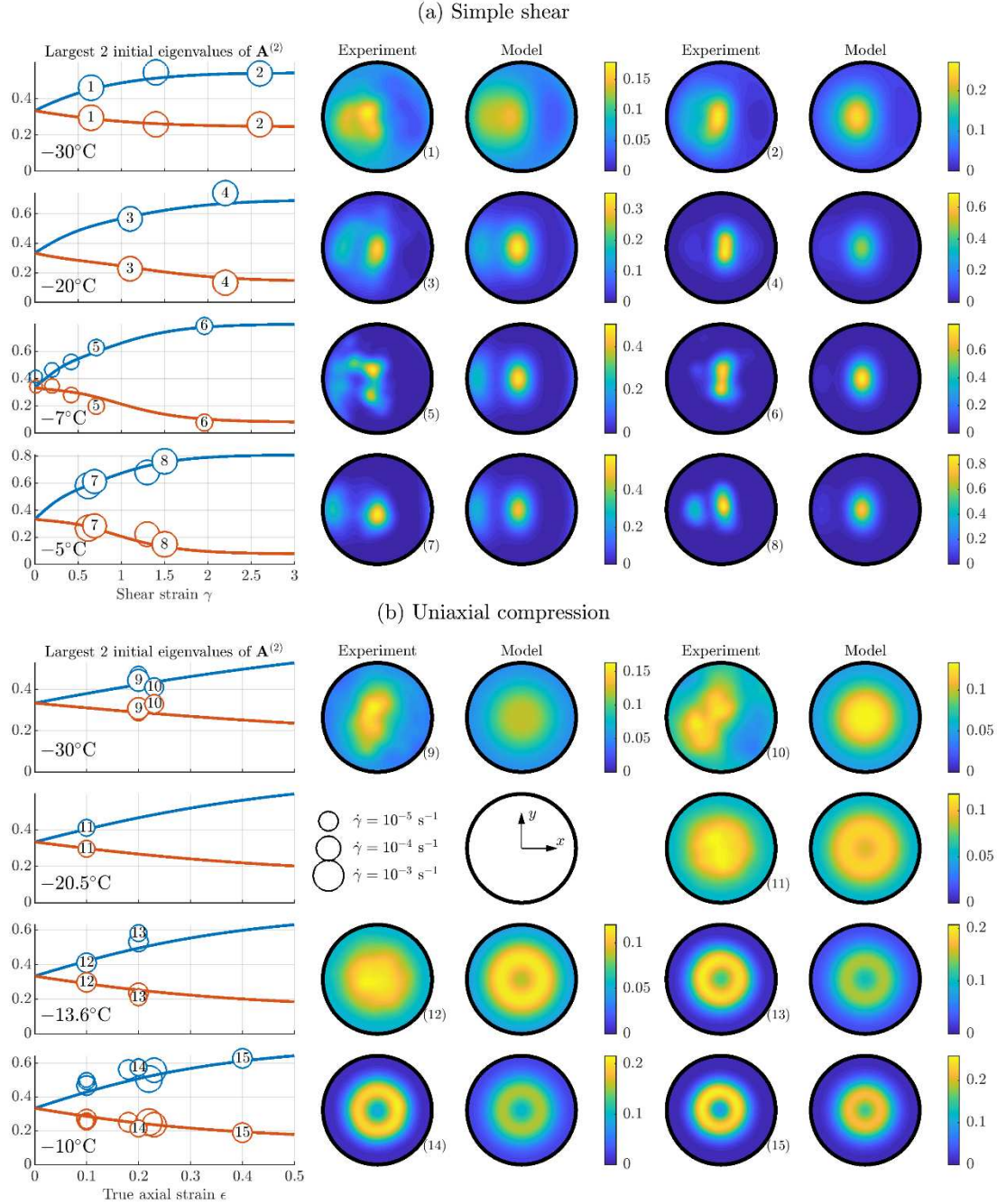
Figure 5: Comparison of the model with experiments performed in (a) simple shear (Journaux et al., 2019; Qi et al., 2019) and (b) compression (Craw et al., 2018; Piazolo et al., 2013). The simulation parameters $(\tilde{\lambda}, \tilde{\beta}, \iota)$ as functions of temperature were taken from the linear regression in Figure 4. Each row shows the comparison between the model and experiments at a specific temperature (and flow field). The first column shows a plot of the largest 2 eigenvalues of $\mathbf{A}^{(2)}$. The line represents the simulation and the circles show experimental values, with their size corresponding to the strain rate at which they took place. The circles with numbers correspond to plotted experimental pole figures. These are shown alongside pole

figures from the model at the same strain. In the top right, the J index for each pole figure is shown, above the number corresponding to the experimental point shown in the plot of $\boldsymbol{A}^{(2)}$. Table 2 shows the experimental conditions. The model was run with the spherical harmonics truncated at L = 12.
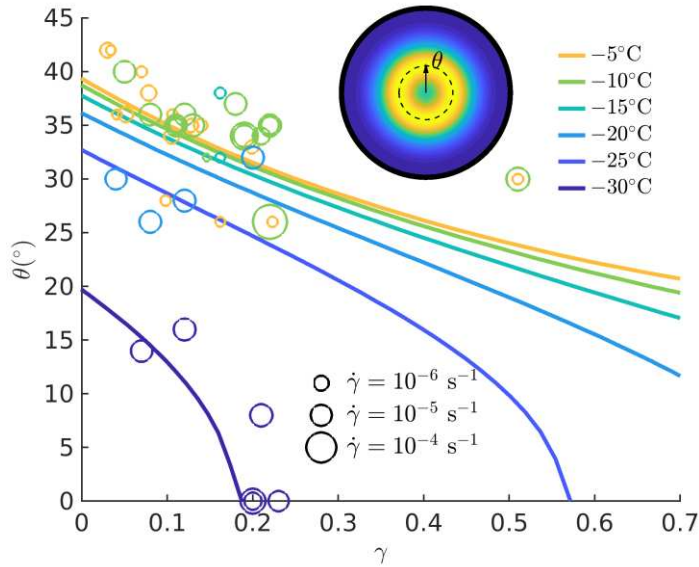
Figure 6: Comparison of model predictions and experimental data showing cone angle θ of the CPO in compression (illustrated in the inset pole figure) against strain γ. Solid lines show results from models run at different temperatures using interpolated parameters as shown in Figure 5. This figure is and adjusted to include the results from our model. Experimental data points are shown as circles taken from experiments (Craw et al., 2018; Fan et al., 2020; Jacka, 2000; Jacka and Maccagnan, 1984; Montagnat et al., 2015; Piazolo et al., 2013; Qi et al., 2017; Vaughan et al., 2017). The size of the marker corresponds to the strain rate the experiment was performed at, and it is coloured by temperature. Representation chosen and experimental data based on fig 14 and table 4 in Fan et al. (2020).

Flow	$T/^\circ$ C	$\dot{\gamma}/\mathrm{s}^{-1}$	n	$c_v(T)$ /%	$c_v(\dot{\gamma})$ /%	$\tilde{\lambda}$	ι	$\tilde{\beta}$
	-30.0	1.26×10^{-5}	3	0.00	107	0.173	1.23	0.620
	-13.6	7.50×10^{-6}	3	0.00	57.7	0.198	1.93	4.25
Compression	-10.2	1.03×10^{-5}	3	8.90	5.60	0.126	1.54	5.92
	-9.50	1.66×10^{-4}	2	3.00	64.5	0.343	1.98	2.75
	-30.3	1.33×10^{-4}	3	1.20	8.60	0.153	0.993	0.763
Simple shear	-7.00	1.14×10^{-6}	5	0.00	71.9	0.139	1.65	4.12
	-5.50	1.26×10^{-4}	4	3.50	33.3	0.178	1.59	5.51

							95% confidence interval		
Variable	Equation	m	c	p	R^2	R^2_{adj}	m	c	p
$\tilde{\lambda}$		0.001	0.21	-	0.033	-0.16	-0.007 - 0.009	0.065 - 0.347	-
ι	$mT + c$	0.026	1.95	-	0.60	0.53	0.002 - 0.050	1.516 - 2.390	-
$\tilde{\beta}$		0.176	6.09	-	0.76	0.71	0.063 - 0.289	4.046 - 8.125	-
$\tilde{\lambda}$		0.007	0.80	0.124	0.37	0.056	-0.025 - 0.039	-1.221 - 2.823	-0.119 - 0.368
ι	$(mT + c)\dot{\gamma}^p$	0.027	2.00	0.002	0.60	0.41	-0.017 - 0.071	-0.252 - 4.260	-0.097 - 0.102
$\tilde{\beta}$		0.144	4.98	- 0.018	0.77	0.65	-0.155 - 0.443	-4.802 - 14.76	-0.193 - 0.156

Table 1: Table showing both the results from the inversion for parameters and the regression. The inversion was performed for 7 bins in total, each with a mean temperate and strain rate. The coefficient of variance is also shown, along with the parameters. The lower table shows the results from the regression, both with and without strain rate dependence. The R^2 and adjusted R^2 values are also shown, along with the 95% confidence intervals for each fitted parameter.
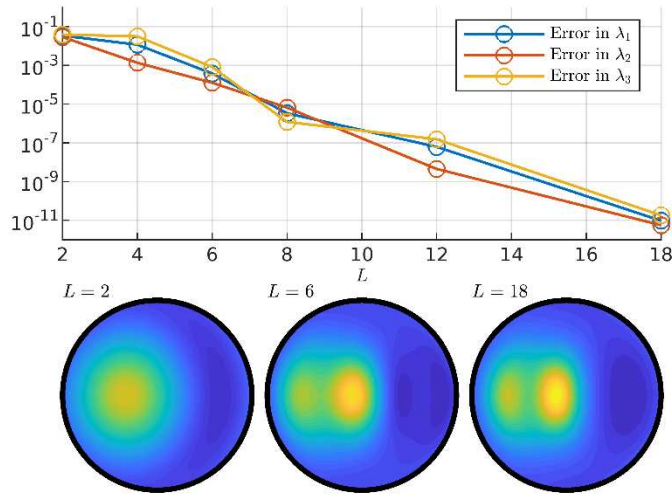
Figure 7: (Appendix) The error in the eigenvalues of $\boldsymbol{A}^{(2)}$ and corresponding pole figures for different values of the number of spectral modes L, illustrating the higher resolution arising for large L. The illustrative parameters $\tilde{\lambda} = 0.05, \iota = 1, \tilde{\beta} = 1$ were chosen here. Both the error and the pole figures are shown at an arbitrary strain of $\gamma = 1$. The error is calculated relative to a highly resolved solution with $L = 50$. The plot shows the exponential convergence of the spectral method.

Experiment	Paper	Name	Flow	$T/°C$	$\dot{\gamma}/s^{-1}$	γ
1		PIL143		-30.6	1.46×10^{-4}	0.65
2	Qi et al.	PIL135		-30.5	1.25×10^{-4}	2.6
3	(2019)	PIL145		-20.1	9.49×10^{-5}	1.1
4		PIL144	Simple shear	-20.4	1.19×10^{-4}	2.2
5	Journaux et al.	TGI071		-7	1.80×10^{-6}	0.71
6	(2019)	TGI196		-7	2.10×10^{-6}	1.96
7	Qi et al.	PIL82		-5.4	7.98×10^{-5}	0.69
8	(2019)	PIL94		-5.2	1.37×10^{-4}	1.5
9	Craw et al.	PIL132		-30	2.80×10^{-5}	0.2
10	(2018)	PIL141		-30	7.20×10^{-6}	0.23
11		13_22		-20.5	2.50×10^{-6}	0.1
12	Piazolo et al.	13_26	Compression	-13.6	1.00×10^{-5}	0.1
13	(2013)	MD9		-13.6	2.50×10^{-6}	0.2
14		MD3		-10.7	2.50×10^{-6}	0.2
15		MD22		-10.7	1.00×10^{-5}	0.4

Table 2: (Appendix) Table showing the experimental data used in Figure 5. The first column gives the experimental number shown in the plot of $A^{(2)}$ and beside the experimental pole figures in Figure 5. This is followed by the paper the data was published in and the conditions the experiment was run at.

References

Azuma, N., Higashi, A., 1984. Mechanical Properties of Dye 3 Greenland Deep Ice Cores. Ann. Glaciol. 5, 1–8. https://doi.org/10.3189/1984AoG5-1-1-8

Bargmann, S., Seddik, H., Greve, R., 2012. Computational modeling of flow-induced anisotropy of polar ice for the EDML deep drilling site, Antarctica: The effect of rotation recrystallization and grain boundary migration. Int. J. Numer. Anal. Methods Geomech. 36, 892–917. https://doi.org/10.1002/nag.1034

Boehler, R., 1996. Melting temperature of the Earth's mantle and core: Earth's thermal structure. Annu. Rev. Earth Planet. Sci. 24, 15–40. https://doi.org/10.1146/annurev.earth.24.1.15

Chauve, T., Montagnat, M., Piazolo, S., Journaux, B., Wheeler, J., Barou, F., Mainprice, D., Tommasi, A., 2017. Non-basal dislocations should be accounted for in simulating ice

mass flow. Earth Planet. Sci. Lett. 473, 247–255.
https://doi.org/10.1016/j.epsl.2017.06.020

Cornford, S.L., Martin, D.F., Graves, D.T., Ranken, D.F., Le Brocq, A.M., Gladstone, R.M., Payne, A.J., Ng, E.G., Lipscomb, W.H., 2013. Adaptive mesh, finite volume modeling of marine ice sheets. J. Comput. Phys. 232, 529–549.
https://doi.org/10.1016/j.jcp.2012.08.037

Craw, L., Qi, C., Prior, D.J., Goldsby, D.L., Kim, D., 2018. Mechanics and microstructure of deformed natural anisotropic ice. J. Struct. Geol. 115, 152–166.
https://doi.org/10.1016/j.jsg.2018.07.014

Cyprych, D., Piazolo, S., Wilson, C.J.L., Luzin, V., Prior, D.J., 2016. Rheology, microstructure and crystallographic preferred orientation of matrix containing a dispersed second phase: Insight from experimentally deformed ice. Earth Planet. Sci. Lett. 449, 272–281. https://doi.org/10.1016/j.epsl.2016.06.010

Drury, M.R., Urai, J., 1990. Deformation-related recrystallization process. Tectonophysics 172, 235–253. https://doi.org/10.1016/0040-1951(90)90033-5

Duval, P., Montagnat, M., Grennerat, F., Weiss, J., Meyssonnier, J., Philip, A., 2010. Creep and plasticity of glacier ice: a material science perspective. J. Glaciol. 56, 1059–1068.
https://doi.org/10.3189/002214311796406185

Fan, S., Hager, T., Prior, D.J., Cross, A.J., Goldsby, D.L., Qi, C., Negrini, M., Wheeler, J., 2020. Temperature and strain controls on ice deformation mechanisms: insights from the microstructures of samples deformed to progressively higher strains at $-$10, $-$20 and $-$30\,$^{\circ}$C. Cryosphere Discuss 2020, 1–43.
https://doi.org/10.5194/tc-2020-2

Faria, S.H., 2006. Creep and recrystallization of large polycrystalline masses. I. General continuum theory. Proc. R. Soc. Math. Phys. Eng. Sci. 462, 1493.
https://doi.org/10.1098/rspa.2005.1610

Faria, S.H., 2001. Mixtures with continuous diversity: general theory and application to polymer solutions. Contin. Mech. Thermodyn. 13, 91–120.
https://doi.org/10.1007/s001610100043

Faria, S.H., Kremer, G.M., Hutter, K., 2008. Reply to Gagliardini's comment on 'Creep and recrystallization of large polycrystalline masses' by Faria and co-authors. Proc. R. Soc. Math. Phys. Eng. Sci. 464. https://doi.org/10.1098/rspa.2008.0181

Faria, S.H., Weikusat, I., Azuma, N., 2014. The microstructure of polar ice. Part II: State of the art. Microdynamics Ice 61, 21–49. https://doi.org/10.1016/j.jsg.2013.11.003

Gagliardini, O., Gillet-Chaulet, F., Montagnat, M., 2009. A Review of Anisotropic Polar Ice Models: from Crystal to Ice-Sheet Flow Models. Phys. Ice Core Rec. II 68.

Gagliardini, O., Zwinger, T., Gillet-Chaulet, F., Durand, G., Favier, L., de Fleurian, B., Greve, R., Malinen, M., Martín, C., R\a aback, P., Ruokolainen, J., Sacchettini, M., Schäfer, M., Seddik, H., Thies, J., 2013. Capabilities and performance of Elmer/Ice, a new-

generation ice sheet model. Geosci. Model Dev. 6, 1299–1318. https://doi.org/10.5194/gmd-6-1299-2013

Gödert, G., 2003. A mesoscopic approach for modelling texture evolution of polar ice including recrystallization phenomena. Ann. Glaciol. 37, 23–28. https://doi.org/10.3189/172756403781815375

Gödert, G., Hutter, K., 1998. Induced anisotropy in large ice shields: theory and its homogenization. Contin. Mech. Thermodyn. 10, 293–318. https://doi.org/10.1007/s001610050095

Jacka, T.H., 2000. Flow rates and crystal orientation fabrics in compression of polycrystalline ice at low temperatures and stresses. Phys. Ice Core Rec.

Jacka, T.H., Maccagnan, M., 1984. Ice crystallographic and strain rate changes with strain in compression and extension. Cold Reg. Sci. Technol. 8, 269–286. https://doi.org/10.1016/0165-232X(84)90058-2

Journaux, B., Chauve, T., Montagnat, M., Tommasi, A., Barou, F., Mainprice, D., Gest, L., 2019. Recrystallization processes, microstructure and crystallographic preferred orientation evolution in polycrystalline ice during high-temperature simple shear. The Cryosphere 13, 1495–1511. https://doi.org/10.5194/tc-13-1495-2019

Kennedy, J.H., Pettit, E.C., 2015. The response of fabric variations to simple shear and migration recrystallization. J. Glaciol. 61, 537–550. https://doi.org/10.3189/2015JoG14J156

Kronenberg, A.K., Kirby, S.H., Pinkston, J., 1990. Basal slip and mechanical anisotropy of biotite. J. Geophys. Res. Solid Earth 95, 19257–19278. https://doi.org/10.1029/JB095iB12p19257

Larour, E., Seroussi, H., Morlighem, M., Rignot, E., 2012. Continental scale, high order, high spatial resolution, ice sheet modeling using the Ice Sheet System Model (ISSM). J. Geophys. Res. Earth Surf. 117. https://doi.org/10.1029/2011JF002140

Lipscomb, W., Price, S., Hoffman, M., Leguy, G., Bennett, A., Bradley, S., Evans, K., Fyke, J., Kennedy, J., Perego, M., Ranken, D., Sacks, W., Salinger, A., Vargo, L., Worley, P., 2018. Description and Evaluation of the Community Ice Sheet Model (CISM) v2.1. Geosci. Model Dev. Discuss. 1–65. https://doi.org/10.5194/gmd-2018-151

Llorens, M.-G., Griera, A., Bons, P.D., Lebensohn, R.A., Evans, L.A., Jansen, D., Weikusat, I., 2016. Full-field predictions of ice dynamic recrystallisation under simple shear conditions. Earth Planet. Sci. Lett. 450, 233–242. https://doi.org/10.1016/j.epsl.2016.06.045

Minchew, B., Meyer, C., Robel, A., Gudmundsson, G., Simons, M., 2018. Processes controlling the downstream evolution of ice rheology in glacier shear margins: case study on Rutford Ice Stream, West Antarctica. J. Glaciol. 64, 1–12. https://doi.org/10.1017/jog.2018.47

Montagnat, M., Castelnau, O., Bons, P.D., Faria, S.H., Gagliardini, O., Gillet-Chaulet, F., Grennerat, F., Griera, A., Lebensohn, R.A., Moulinec, H., Roessiger, J., Suquet, P., 2014.

Multiscale modeling of ice deformation behavior. Microdynamics Ice 61, 78–108. https://doi.org/10.1016/j.jsg.2013.05.002

Montagnat, M., Chauve, T., Barou, F., Tommasi, A., Beausir, B., Fressengeas, C., 2015. Analysis of Dynamic Recrystallization of Ice from EBSD Orientation Mapping. Front. Earth Sci. 3, 81. https://doi.org/10.3389/feart.2015.00081

Montgomery-Smith, S., Jack, D.A., Smith, D.E., 2010. A systematic approach to obtaining numerical solutions of Jeffery's type equations using Spherical Harmonics. Compos. Part Appl. Sci. Manuf. 41, 827–835. https://doi.org/10.1016/j.compositesa.2010.02.010

Nicolas, A., Christensen, N.I., 1987. Formation of Anisotropy in Upper Mantle Peridotites - A Review, in: Composition, Structure and Dynamics of the Lithosphere-Asthenosphere System. American Geophysical Union (AGU), pp. 111–123. https://doi.org/10.1029/GD016p0111

Ossipyan, Yu.A., Petrenko, V., 1988. The Physics of Ice. Europhys. News 19, 61–64. https://doi.org/10.1051/epn/19881905061

Paterson, W.S.B., 1999. The Physics of Glaciers, 3rd ed. Pergamon, Oxford.

Piazolo, S., Wilson, C.J.L., Luzin, V., Brouzet, C., Peternell, M., 2013. Dynamics of ice mass deformation: Linking processes to rheology, texture, and microstructure. Geochem. Geophys. Geosystems 14, 4185–4194. https://doi.org/10.1002/ggge.20246

Pimienta, P., Duval, P., 1987. Mechanical behavior of anisotropic polar ice. Phys. Basis Ice Sheet Model. 170.

Placidi, L., Greve, R., Seddik, H., Faria, S.H., 2010. Continuum-mechanical, Anisotropic Flow model for polar ice masses, based on an anisotropic Flow Enhancement factor. Contin. Mech. Thermodyn. 22, 221–237. https://doi.org/10.1007/s00161-009-0126-0

Placidi, L., Hutter, K., 2006. Thermodynamics of polycrystalline materials treated by the theory of mixtures with continuous diversity. Contin. Mech. Thermodyn. 17, 409. https://doi.org/10.1007/s00161-005-0006-1

Qi, C., Goldsby, D.L., Prior, D.J., 2017. The down-stress transition from cluster to cone fabrics in experimentally deformed ice. Earth Planet. Sci. Lett. 471, 136–147. https://doi.org/10.1016/j.epsl.2017.05.008

Qi, C., Prior, D.J., Craw, L., Fan, S., Llorens, M.-G., Griera, A., Negrini, M., Bons, P.D., Goldsby, D.L., 2019. Crystallographic preferred orientations of ice deformed in direct-shear experiments at low temperatures. The Cryosphere 13, 351–371. https://doi.org/10.5194/tc-13-351-2019

Schmid, S.M., Casey, M., 1986. Complete Fabric Analysis of Some Commonly Observed Quartz C-Axis Patterns, in: Mineral and Rock Deformation. American Geophysical Union (AGU), pp. 263–286. https://doi.org/10.1029/GM036p0263

Seddik, H., Greve, R., Placidi, L., Hamann, I., Gagliardini, O., 2008. Application of a continuum-mechanical model for the flow of anisotropic polar ice to the EDML core, Antarctica. J. Glaciol. 54, 631–642. https://doi.org/10.3189/002214308786570755

Seddik, H., Greve, R., Zwinger, T., Placidi, L., 2011. A full Stokes ice flow model for the vicinity of Dome Fuji, Antarctica, with induced anisotropy and fabric evolution. The Cryosphere 5, 495–508. https://doi.org/10.5194/tc-5-495-2011

Shepherd, A., Ivins, E., Rignot, E., Smith, B., van den Broeke, M., Velicogna, I., Whitehouse, P., Briggs, K., Joughin, I., Krinner, G., Nowicki, S., Payne, T., Scambos, T., Schlegel, N., A, G., Agosta, C., Ahlstrøm, A., Babonis, G., Barletta, V., Blazquez, A., Bonin, J., Csatho, B., Cullather, R., Felikson, D., Fettweis, X., Forsberg, R., Gallee, H., Gardner, A., Gilbert, L., Groh, A., Gunter, B., Hanna, E., Harig, C., Helm, V., Horvath, A., Horwath, M., Khan, S., Kjeldsen, K.K., Konrad, H., Langen, P., Lecavalier, B., Loomis, B., Luthcke, S., McMillan, M., Melini, D., Mernild, S., Mohajerani, Y., Moore, P., Mouginot, J., Moyano, G., Muir, A., Nagler, T., Nield, G., Nilsson, J., Noel, B., Otosaka, I., Pattle, M.E., Peltier, W.R., Pie, N., Rietbroek, R., Rott, H., Sandberg-Sørensen, L., Sasgen, I., Save, H., Scheuchl, B., Schrama, E., Schröder, L., Seo, K.-W., Simonsen, S., Slater, T., Spada, G., Sutterley, T., Talpe, M., Tarasov, L., van de Berg, W.J., van der Wal, W., van Wessem, M., Vishwakarma, B.D., Wiese, D., Wouters, B., The IMBIE team, 2018. Mass balance of the Antarctic Ice Sheet from 1992 to 2017. Nature 558, 219–222. https://doi.org/10.1038/s41586-018-0179-y

Shoji, H., Langway, C.C., 1988. Flow-Law Parameters of the Dye 3, Greenland, Deep Ice Core. Ann. Glaciol. 10, 146–150. https://doi.org/10.3189/S026030550000433X

Svendsen, B., Hutter, K., 1996. A continuum approach for modelling induced anisotropy in glaciers and ice sheets. Ann. Glaciol. 23, 262–269. https://doi.org/10.3189/S0260305500013525

Tommasi, A., Knoll, M., Vauchez, A., Signorelli, J.W., Thoraval, C., Logé, R., 2009. Structural reactivation in plate tectonics controlled by olivine crystal anisotropy. Nat. Geosci. 2, 423–427. https://doi.org/10.1038/ngeo528

van der Veen, C.J., Whillans, I.M., 1994. Development of fabric in ice. Cold Reg. Sci. Technol. 22, 171–195. https://doi.org/10.1016/0165-232X(94)90027-2

Vaughan, M.J., Prior, D.J., Jefferd, M., Brantut, N., Mitchell, T.M., Seidemann, M., 2017. Insights into anisotropy development and weakening of ice from in situ P wave velocity monitoring during laboratory creep. J. Geophys. Res. Solid Earth 122, 7076–7089. https://doi.org/10.1002/2017JB013964

Wilson, C., Hunter, N., Luzin, V., Peternell, M., Piazolo, S., 2019. The influence of strain rate and presence of dispersed second phases on the deformation behaviour of polycrystalline D2O ice. J. Glaciol. 65, 101–122. https://doi.org/10.1017/jog.2018.100

Winkelmann, R., Martin, M.A., Haseloff, M., Albrecht, T., Bueler, E., Khroulev, C., Levermann, A., 2011. The Potsdam Parallel Ice Sheet Model (PISM-PIK) – Part 1: Model description. The Cryosphere 5, 715–726. https://doi.org/10.5194/tc-5-715-2011